



Universiteit
Leiden
The Netherlands

Efficient and realistic simulation of phase coexistence

Sevink, G.J.A.; Blokhuis, E.M.; Li, X.; Milano, G.

Citation

Sevink, G. J. A., Blokhuis, E. M., Li, X., & Milano, G. (2020). Efficient and realistic simulation of phase coexistence. *Journal Of Chemical Physics*, 153(24), 244121. doi:10.1063/5.0027778

Version: Publisher's Version

License: [Leiden University Non-exclusive license](#)

Downloaded from: <https://hdl.handle.net/1887/139159>

Note: To cite this publication please use the final published version (if applicable).

Efficient and realistic simulation of phase coexistence

Cite as: J. Chem. Phys. **153**, 244121 (2020); <https://doi.org/10.1063/5.0027778>

Submitted: 31 August 2020 . Accepted: 03 December 2020 . Published Online: 29 December 2020

 G. J. A. Sevink,  E. M. Blokhuis,  X. Li, and  G. Milano



View Online



Export Citation



CrossMark

ARTICLES YOU MAY BE INTERESTED IN

[Effect of the range of particle cohesion on the phase behavior and thermodynamic properties of fluids](#)

The Journal of Chemical Physics **153**, 244502 (2020); <https://doi.org/10.1063/5.0031517>

[MDBenchmark: A toolkit to optimize the performance of molecular dynamics simulations](#)

The Journal of Chemical Physics **153**, 144105 (2020); <https://doi.org/10.1063/5.0019045>

[Eyring equation and fluctuation–dissipation far away from equilibrium](#)

The Journal of Chemical Physics **153**, 244116 (2020); <https://doi.org/10.1063/5.0032634>



New

Your Qubits. Measured.

Meet the next generation of quantum analyzers

- Readout for up to 64 qubits
- Operation at up to 8.5 GHz, mixer-calibration-free
- Signal optimization with minimal latency

Find out more



Efficient and realistic simulation of phase coexistence

Cite as: J. Chem. Phys. 153, 244121 (2020); doi: 10.1063/5.0027778

Submitted: 31 August 2020 • Accepted: 3 December 2020 •

Published Online: 29 December 2020



View Online



Export Citation



CrossMark

G. J. A. Sevink,^{1,a)} E. M. Blokhuis,¹ X. Li,^{1,3} and G. Milano³

AFFILIATIONS

¹Leiden Institute of Chemistry, Leiden University, P.O. Box 9502, 2300 RA Leiden, The Netherlands

²Theoretical Physical Chemistry, Organic Materials Modeling, Department of Organic Materials Science, Yamagata University, 4-3-16 Jonan, Yonezawa, Yamagata-ken 992-8510, Japan

³Department of Chemistry and Hylleraas Centre for Quantum Molecular Sciences, University of Oslo, P.O. Box 1033 Blindern, 0315, Oslo, Norway

^{a)}Author to whom correspondence should be addressed: a.sevink@chem.leidenuniv.nl

ABSTRACT

We show how an existing concurrent multi-scale method named hybrid particle field-molecular dynamics (hPF-MD) can be adapted to enable the simulation of structure and/or structural dynamics in compressible systems. Implementing such new equations of state (EOS) into hPF-MD, while conserving the efficiency associated with treating intermolecular interactions in a continuum fashion, opens this method up to describe a new class of phenomena in which non-uniform densities play a role, for example, evaporation and crystallization. We carefully consider how compressible hPF-MD compares to its mean-field counterpart for two particular EOS, adopted from the Cell Model for polymers and the Carnahan–Starling expression for hard spheres. Here, we performed a very basic analysis for a single-component system, focusing on the significance of various particle-based parameters and the particle-to-field projection. Our results illustrate the key role of the particle density per field grid cell and show that projection based on a Gaussian kernel is preferred over the standard cloud-in-cell projection. They also suggest that the behavior of hPF-MD close to the critical point is non-classical, i.e., in agreement with a critical exponent for a pure particle description, despite the mean-field origin of the method.

Published under license by AIP Publishing. <https://doi.org/10.1063/5.0027778>

I. INTRODUCTION

Most of the conventional computational methods that are capable of describing structuring and structure formation in multi-component systems at the mesoscale, for instance, dissipative particle dynamics (DPD) and self-consistent field (SCF) theory, are incapable of describing liquid–liquid or liquid–vapor coexistence in a single-component or “pure” system. The origin of this limitation is hidden in the representation of the excluded volume interactions by a Helfand penalty term for nearly incompressible systems in SCF or by (purely repulsive) interparticle forces in DPD that are linearly dependent on the particle separation distance. As both choices give rise to a *quadratic* equation of state (EOS) for pressure in terms of the density, they lack the necessary van der Waals loop. Various experimental phenomena, however, involve phase coexistences,

with prominent examples in polymeric systems being the solvent evaporation that takes place upon thermal annealing of spin-coated block copolymer films, which may particularly affect microstructure orientation, and the coexistence of liquid ordered and disordered phases in lipid membranes. A pragmatic but not necessarily accurate work-around for simulating evaporation phenomena by conventional DPD or SCF is the introduction of an “air” component, either in terms of particles or a field, with the excluded volume interactions of a solvent.

In a seminal paper that appeared in 2001, Pagonabarraga and Frenkel¹ introduced a hybridization procedure to set up simulations within the DPD framework according to a preferred EOS, in their case the ones associated with a van der Waals fluid and that of a binary mixture. To do so, they introduced interactions that depend on a local excess free energy in terms of smoothed

density fields, which can be extracted from the (local) particle structure via an appropriate projection scheme. The projection that they considered is natural in the sense that it agrees with a well-known procedure in field-theoretic modeling in which densities are obtained from instantaneous particle configurations via the microscopic density operator. However, to introduce an effective volume for individual (DPD) particles, they replaced the standard δ -functions by normalized weight functions $w(\mathbf{r})$, which has the effect of smoothing the density. The name “multibody” or “many-body” DPD (MDPD), particularly referring to the mean-field aspects of this approach, was soon after (2002) attributed to the method by Trofimov,² who proposed a way to capture the effect of particle correlations that are absent in the original MDPD method, but are of particular significance in stronger non-ideal systems for which the method was designed. By matching MDPD simulation results with the target (mean-field) EOS, which includes multi-body effects by construction, their self-consistent scheme is able to iteratively determine corrections to the densities obtained from the original projection scheme of Pagonabarraga and Frenkel.¹ They illustrated the success of their approach by reproducing phase behavior for a Lennard-Jones (LJ) fluid and a compressible Huggins fluid.

Next, in 2003, Warren³ published a study that provided a new interpretation of MDPD. By splitting the conservative forces into purely attractive and density-dependent repulsive contributions, he obtained an EOS of third order in the density that contains a van der Waals loop. The weight functions used for the conservative MDPD forces and for the density assignment turn out to be related, meaning that they cannot be chosen independently, and he introduced different ranges for the attractive and repulsive interactions in order to stabilize the liquid–vapor interface, which he validated by simulating a pendant droplet. Although not illustrated, the use of Trofimov’s approach for correcting the assignment scheme toward reproduction of the mean-field EOS remains an option. The equivalence of liquid–vapor interface properties calculated using the MDPD approach of Warren³ and Multi-body Monte Carlo (MMC) was reported by Ghoufi and Malfreyt.⁴ They showed that the contribution of the repulsive part of the conservative forces to the total surface tension is rather sensitive to the range of these density-dependent interactions, thereby highlighting the sensitivity to this parameter.

The community that describes structure formation and dynamics in polymeric materials by field-theoretic models has also explored the opposite direction, i.e., to hybridize (mean-field) SCF methodology by the introduction of molecular details. As with MDPD, we only shortly review principal directions, noting that most generally applicable hybrid descriptions have started from a mean-field free energy for (nearly) incompressible systems such as polymers, i.e., based on the conventional treatment of excluded volume interactions. Among the class of methods that aim at incorporating fluctuations in a mean-field description, the Single Chain in Mean Field (SCMF) method of Daoulas and Müller^{5,6} employs a Monte Carlo (MC) technique to update particle-based chain conformations until their projected densities are consistent with (external) potentials that are derived from such a mean-field (SCF) free energy. It is also the starting point for the hybrid MD-SCF method that Kawakatsu and Milano⁷ introduced in 2009, which employs similar potentials but, unlike SCMF, evolves particle-based systems via Newton’s equations of motion, replacing “hard” non-bonded interaction forces by much

“softer” forces that are obtained as spatial derivatives of field-based potentials. To avoid confusion between classical mean-field SCF and these newer hybrid approaches, we adopt the recently introduced acronym hPF-MD (hybrid particle field method-molecular dynamics) for MD-SCF, and we acknowledge these two principle directions in hybrid particle-field modeling by further referring to the method of Daoulas and Müller as hPF-MC. Both hPF approaches have been successfully applied to simulate structure formation and structural processes in polymeric and lipidic systems. An interesting but more particular development considers incorporating the effect of molecular-scale density correlations into the van der Waals theory for the liquid–vapor interface, as set forward in a series of papers by Katsov, Weeks, and coworkers.⁸

While MDPD and the hPF approaches are conceptually closely linked, they do inherit properties from their parent techniques. Numerical evaluation of continuum theories such as SCF requires the introduction of a computational grid, which, in addition to general issues such as the isotropy and precision of finite difference (FD) operators, introduces a sensitivity to the chosen projection scheme. In particular, whereas the pairwise interactions and the density assignment in MDPD are translationally invariant, the projection scheme in hPF methods usually does not satisfy this property. As a consequence, particles may experience anomalous self-interactions,¹¹ which appears to be the reason why hPF applications have thus far focused on dense, nearly incompressible systems for which this effect is less relevant and a quadratic density functional representation of excluded volume interactions is appropriate. Nevertheless, higher-order density functionals that are capable of representing liquid–vapor coexistences have been considered within the hPF-MC approach for studying phenomena in polymeric and amphiphilic systems in which density variations do play a key role.^{5,9,10} Yet, in 2010, Homberg and Müller considered a third order density functional and MDPD, rather than hPF-MC, to evaluate a liquid-to-gel transition in a single-component lipid bilayer membrane.^{12,13} Moreover, in contrast to taking the standard quadratic weight functions in combination with different ranges for the attractive and repulsive interactions proposed by Warren,³ they proposed to consider another weight function for the attractive term and equal ranges for all interactions. The apparent trade-off with hPF, however, is the need for setting up neighbor lists to evaluate the density projection and pairwise interactions, which renders MDPD computationally much less favorable than hPF.¹⁴

In the present study, we propose new hybrid particle-field Hamiltonians for compressible systems, which give rise to compressible hPF-MD or c-hPF-MD that couples efficiency to the ability to simulate phase coexistences. We do so by replacing the conventional harmonic Helfand term for excluded volume interactions by a term that introduces higher order contributions of the density in the equation of state for the pressure, inspired by the excess free energy with respect to an ideal gas.¹⁵ We considered two existing expressions: one adopted from the Cell Model (CM) for polymer melts and another from the Carnahan–Starling (CS) model for hard spheres, but, in principle, any excluded volume term that relates to a desired EOS could be implemented. We particularly focus on investigating the role of the projection scheme, which is a key issue in hPF approaches for a much broader range of applications. Finally, we evaluate the role of hybridization in the phase behavior for our new c-hPF-MD method.

II. THEORY

A. The hPF-MD method

For algorithmic and/or technical details of hPF-MD, or MD-SCF as it is referred to in older publications, we refer to published work. Here, we only repeat the essentials, and note that this method follows the SCF philosophy for treating the intermolecular interactions, by replacing “hard” Lennard-Jones interactions between particles by “soft” mean-field interactions between particle concentration fields, while treating the intramolecular interactions associated with particles in a molecule in the spirit of MD. For reasons of consistency, we adopt the existing notations as much as possible. In the hybrid approach of hPF-MD, the interaction term for the non-bonded interactions between molecules is given by

$$W[\{\rho_K(\mathbf{r})\}] = F^c[\{\rho_K(\mathbf{r})\}] + F^e[\{\rho_K(\mathbf{r})\}], \quad (1)$$

with F^c and F^e containing the cohesive and excluded volume interactions given by

$$F^c[\{\rho_K(\mathbf{r})\}] = \frac{1}{2} \int_V \sum_{KK'} \chi_{KK'} \rho_K(\mathbf{r}) \rho_{K'}(\mathbf{r}) d\mathbf{r}, \quad (2)$$

$$F^e[\{\rho_K(\mathbf{r})\}] = \frac{\kappa_H}{2} \int_V \left(\sum_K \rho_K(\mathbf{r}) - \rho_0 \right)^2 d\mathbf{r}, \quad (3)$$

where V is the (simulation) volume, $\rho_K(\mathbf{r})$ is the particle density for particles of type K at position \mathbf{r} , and $\chi_{KK'} = \chi_{K'K}$ is an interaction matrix that has the dimension of energy times volume. The expression in (2) is the familiar Flory–Huggins parameter to describe mean-field cohesive interactions between concentration fields labeled by particle types K and K' .

The second term in (1), i.e., the Helfand penalty function (3), relates to the compressibility of the system, which should be constrained when simulating liquids. Penalizing deviations from a constant background value $\rho_0 = \int_V \sum_K \rho_K(\mathbf{r}) d\mathbf{r} / V$ rather than introducing strict constraints on the total mass transfer introduces small variations of the total density field $\sum_K \rho_K$ around this reference value, thereby enabling a control of excluded volume interactions. The strength κ_H , where the subscript H refers to the Helfand origin, is of the same units as χ and sets the tolerated deviation from the constant total number density of segments ρ_0 . Although its value can be estimated based on theoretical considerations, it is usually chosen based on considerations about the permitted (small) amplitude of fluctuations or noise.

In the hybrid approach of hPF-MD, it is essential to realize that the free energy is a functional of the instantaneous distribution of particles (in the form of density fields), which fluctuates over time. Its mean-field character is derived from the assumption that its functional derivative defines a conservative mean-field potential that can be used to calculate forces on each particle from the (fluctuating) surrounding density field. Non-bonded interactions are thus taken into account by introducing this *mean-field* interaction potential

$$\begin{aligned} V_K(\mathbf{r}) &= \frac{\delta(W[\{\rho_K(\mathbf{r})\}])}{\delta\rho_K(\mathbf{r})} \\ &= \sum_{K'} \chi_{KK'} \rho_{K'}(\mathbf{r}) + \kappa_H \left(\sum_K \rho_K(\mathbf{r}) - \rho_0 \right). \end{aligned} \quad (4)$$

The resulting mean-field forces on a particle of type K are then given by

$$\mathbf{F}_K(\mathbf{r}) = -\nabla_{\mathbf{r}} V_K(\mathbf{r}) = -\sum_{K'} (\chi_{KK'} + \kappa_H) \nabla_{\mathbf{r}} \rho_{K'}(\mathbf{r}). \quad (5)$$

If we were to consider a one-component system with a *uniform* particle density $\rho_K(\mathbf{r}) \rightarrow \rho(\mathbf{r}) = n/V$, the pressure of the system is then straightforwardly calculated by considering the volume derivative of the total free energy, $F = F^{id} + W$ with $F^{id} = k_B T n \ln(n\Lambda^3/V)$, giving

$$p = -\left(\frac{\partial F}{\partial V} \right)_{n,T} = k_B T \rho + \frac{1}{2} (\chi + \kappa_H) \rho^2, \quad (6)$$

which one could relate to the isothermal compressibility of water to obtain a realistic estimate for κ_H .

B. Incorporating other equations of state

In this study, we are interested in simulating *compressible* systems, in particular liquid–vapor coexistence. It is then necessary to replace the harmonic Helfand term (3) by a term that introduces higher order density contributions in the equation of state for the pressure. Here, we introduce an interaction term inspired by the excess free energy with respect to an ideal gas¹⁵ and replace the Helfand penalty term in (3) by

$$F^e[\{\rho_K(\mathbf{r})\}] = -k_B T \sum_K \int_V \rho_K(\mathbf{r}) \ln c(\mathbf{r}) d\mathbf{r}, \quad (7)$$

where the functional $c(\mathbf{r})$ represents an insertion probability corresponding to the effective fraction of accessible free space.

In the following, we focus on systems containing only particles of a **single type** with density $\rho(\mathbf{r})$ and consider two known options for the insertion probability $c(\mathbf{r})$ that have not been considered before in the context of hPF,

$$c(\mathbf{r}) = \begin{cases} (1 - \eta^{\frac{1}{3}})^3 & \text{(Cell Model)} \\ e^{-\frac{\eta(4-3\eta)}{(1-\eta)^2}} & \text{(Carnahan–Starling),} \end{cases} \quad (8)$$

where $\eta = \eta(\mathbf{r})$ is a dimensionless volume fraction related to the density as $\eta(\mathbf{r}) = v\rho(\mathbf{r})$. For more general expressions in the case of multiple particle species, we refer to the work of Maurits *et al.*¹⁵ While the parameter v is introduced as the particle volume, we show that it acts as a scaling factor that restrains the insertion probability $c(\mathbf{r})$ to a certain interval.

To determine the mean-field forces corresponding to these two expressions, we first consider the corresponding interaction potentials,

$$\frac{V^e(\mathbf{r})}{k_B T} = \begin{cases} -\ln(1 - \eta^{\frac{1}{3}})^3 + \frac{\eta}{\eta^{\frac{1}{3}} - \eta} & \text{(CM)} \\ \frac{\eta(4-3\eta)}{(1-\eta)^2} + \frac{4\eta-2\eta^2}{(1-\eta)^3} & \text{(CS).} \end{cases} \quad (9)$$

These expressions give rise to a total force on particles for the Cell Model (CM),

$$\frac{\mathbf{F}(\mathbf{r})}{k_B T} = -\left[\tilde{\chi} + \frac{\frac{4}{3}\eta(\mathbf{r})^{\frac{2}{3}} - \eta(\mathbf{r})}{(\eta(\mathbf{r})^{\frac{2}{3}} - \eta(\mathbf{r}))^2} \right] \nabla_{\mathbf{r}} \eta(\mathbf{r}), \quad (10)$$

and for the Carnahan–Starling (CS) model,

$$\frac{\mathbf{F}(\mathbf{r})}{k_B T} = - \left[\tilde{\chi} + \frac{2(\eta(\mathbf{r}) - 4)}{(1 - \eta(\mathbf{r}))^4} \right] \nabla_{\mathbf{r}} \eta(\mathbf{r}), \quad (11)$$

where we have defined the dimensionless interaction parameter,

$$\tilde{\chi} \equiv \frac{\chi}{k_B T v}. \quad (12)$$

In the original CS model for hard spheres, the free energy is written in terms of the packing fraction and the volume v corresponds to the volume $v = \pi\sigma^3/6$ of a single, spherical hard-sphere particle with diameter σ . The corresponding equation of state for the pressure has shown to provide a good approximation for hard spheres up to $\eta \lesssim 0.55$. Particles in our hPF model, however, possess no intrinsic physical size or volume: they are essentially point particles and there is, in principle, no bound on the number density of the system. The approach in the compressible hPF-MD scheme is then to perform an MD simulation of n particles in a simulation box of volume V so that the overall number density is $\rho_0 = n/V$. The local particle density $\rho(\mathbf{r})$ is obtained by projecting individual particles to a cubic grid with spacing ℓ via a projector scheme that is discussed later on in more detail. As a next step, the density is rescaled by the total density ρ_0 and the volume parameter v to define the dimensionless fraction variable

$$f(\mathbf{r}) \equiv \frac{v\rho(\mathbf{r})}{\ell^3 \rho_0}. \quad (13)$$

In addition to this fraction, also the average particle number per grid cell $\bar{\rho}_0 = \ell^3 \rho_0$ is an important dimensionless parameter that should be conserved when directly comparing different setups. Finally, the force on each particle is calculated replacing $\eta(\mathbf{r}) \rightarrow f(\mathbf{r})$ in either (10) or (11). For a one-phase system, this procedure would lead to the average fraction being equal to $f = \bar{v} = v/\ell^3$, but in a two-phase system, the system phase separates in two regions with average fractions below and above \bar{v} , i.e., $f = f_v$ and $f = f_\ell$. By varying $\tilde{\chi}$, c-hPF-MD can be employed to construct a phase diagram (PD). In this study, we concentrate on the role of hybridization and discretization in this phase behavior and on a comparison with the phase diagrams obtained by regular MD simulations and the corresponding CM or CS mean-field theory.

C. The particle-to-mesh projection

The mean-field potentials needed for the determination of forces on particles due to non-bonded interactions are self-consistently obtained from an instantaneous projection of particles of type K at position \mathbf{r} to a corresponding field $\rho_K(\mathbf{r})$. In computational setups, however, continuum variables or fields are only known on the nodes of a computational grid or mesh, which is usually chosen to be uniformly distributed with spacing ℓ ; these mesh values are consequently employed to evaluate forces on a staggered grid via appropriate finite-difference (FD) gradient operators. Although some projections consider the simplest assignment of particles to the nearest grid point, most hybrid particle-field methods, including hPF-MD, employ an efficient cloud-in-cell (CIC) scheme to assign particle fractions to all the nearest (in 2D: four and in 3D: eight) grid nodes using trilinear interpolation [see Fig. 1(a)]. Yet, a disadvantage of this efficient procedure is that it lacks translational invariance. For instance, a single particle centered in a grid cell would provide $\rho(\blacksquare) = 1/4$ for all four nearest neighbors, while translating the computational grid as a whole by

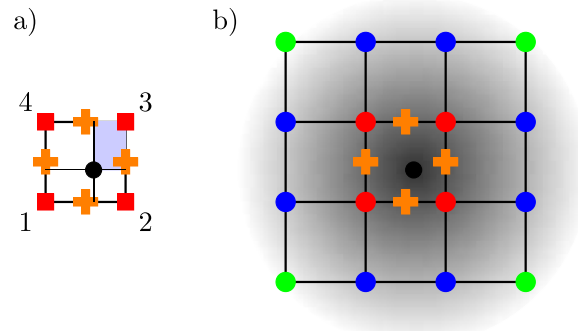


FIG. 1. Schematic (2D) illustration for a single particle (black sphere) of the two considered projection schemes: (a) cloud-in-cell (CIC) scheme in which particle fractions are geometrically assigned to nearest grid nodes (red cubes). As an example, the normalized area of the blue shaded rectangle adjacent to node three is assigned to the opposite node 1. (b) Assignment by Gaussian smearing. Nodes that receive a weighted (normalized) particle fraction are shown by circles: nearest—red, next nearest—blue, and next next nearest—green. In both cases, gradients are computed on a staggered grid (orange) from density values at their nearest (red) nodes.

$\vec{s} = (\ell/2, \ell/2)^T$ would change that in only one $\rho(\blacksquare) = 1$ and all other three $\rho(\blacksquare) = 0$. Although this effect is clearly less significant for dense particle systems, the CIC assignment procedure brings along undesired discretization artifacts or an unphysical introduction of self-interactions.¹⁶

One may, however, also consider other projection schemes. One option is to project and at the same time introduce effective particle volumes via one of the C_1 smoothing kernels proposed in smoothed particle hydrodynamics (SPH). While remaining reasonably local, depending on the choice of the kernel, it has the advantage over the CIC projection that translation invariance is retained and that these kernels can be analytically differentiable. Some of us have previously employed a Gaussian kernel to assign density values $\exp(-d^2/\sigma^2)/\mathcal{N}$ to the 16 (2D) or 64 (3D) grid nodes surrounding each particle, with d being the geometric distance between the particle position and the considered grid node location, $\sigma = \ell$ being the spread, and $\mathcal{N} = \sum_{i \in \{\blacksquare, \blacksquare, \blacksquare, \blacksquare\}} \rho_i$ being an appropriate normalization constant.¹⁷ Although this gives rise to an eightfold increase of the computational effort needed for projection when compared to CIC, it retains the separation between bonded and non-bonded interactions and, thus, the efficiency of parallelization. In particular, since the particle density in the vapor phase will be low, we will consider this projection as well. To enable direct comparison, we will not exploit the analytic differentiability that comes with using Gaussian kernels in this study but instead rely on the existing FD gradient operators. Another, very recent suggestion is to determine densities from the force density,¹⁸

$$\mathbf{F}(\mathbf{r}) = \left\langle \sum_{i=1}^n \delta(\mathbf{r}_i - \mathbf{r}) \mathbf{f}_i \right\rangle, \quad (14)$$

with \mathbf{f}_i being the force acting on particle i using the expression

$$\rho(\mathbf{r}) = \rho_0 + \frac{\beta}{4\pi} \int \frac{\mathbf{r}' - \mathbf{r}}{|\mathbf{r}' - \mathbf{r}|^3} \cdot \mathbf{F}(\mathbf{r}) d\mathbf{r}'. \quad (15)$$

Evaluating this integral in Fourier space would resolve the essential non-locality of (15). Nevertheless, we leave such alternative projection schemes for the future.

Any projection algorithm attributes fractions of each particle to the surrounding grid nodes adding up to one, so the sum of all densities over the computational grid should be given by

$$\sum_{K, \mathbf{r}_k \in \text{grid}} \rho_K(\mathbf{r}_k) = n, \quad (16)$$

if we correctly account for periodic boundaries. Moreover, normalization of this particle density $\rho(\mathbf{r})$ by the average value ρ_0 renders the non-bonded interactions independent of the chosen number of particles n , which is a desired property for any hybrid method that mixes continuum and discrete variables. Yet, we focus on two limiting cases for a fixed volume V .

At the lower limit, i.e., for small n , the vapor fraction f_v may relate to an average number of particles per grid cell in the vapor phase that drops below one, meaning that the discrete particle system is inapt to represent the lowest free energy state in the continuum representation. For this reason, we have to ensure that $\rho(\mathbf{r}) \geq 1/\ell^3$ for the most stable state, which translates into a lower bound $n = n_{\min}$ for which the average number of particles per grid $\tilde{\rho}_0 = \ell^3 n/V = n/\tilde{V}$ satisfies $\tilde{\rho}_0 v_0/\tilde{v} = 1$. For the other extreme, i.e., upon increasing n to a large value n_{\max} , we find that $\tilde{\rho}_0 \rightarrow \infty$. Thus, if we consider the hybrid method a discrete version of the SCF description, both models should give fully consistent results (the continuity condition). Consequently, any realistic choice of $n_{\min} < n < n_{\max}$ that stems from an experimentally measured density should be appropriate but may introduce discretization effects in the field representation, which one may think of as tuning the noise level in the continuum (field) variable. We will consider this relation further in Sec. III.

D. Discrete gradients

Gradients of the density fields are obtained using a finite difference (FD) gradient operator \mathcal{D}_ℓ on a grid that is staggered with respect to the density field grid (see Fig. 1 and previous publications for more details).¹⁹ While FD operators are known to provide an approximate of their continuum counterparts, a direct relation between the discretization error and the grid spacing ℓ should be absent for our system that exhibits no genuine length scale. To quantify this statement, we also considered simulations for a reduced grid spacing and equally reduced time step. For the standard case, $\ell = 1.0$ nm, we usually selected a time step of 0.3 ps, noting that there are only soft non-bonded interactions and that a larger time step will speed up equilibration. We used the original discrete gradient operator of Milano *et al.*¹⁴ A more isotropic operator was recently proposed,¹⁷ but we note that they provide equivalent results for the flat interfaces considered in this study.

An important observation is that the force balance is sensitive to the way the gradients are evaluated. For the considered setup, the attractive forces of (5), i.e., $\mathbf{F}^{\text{att}} = -\nabla(\chi\rho)$, should balance the repulsive forces $\mathbf{F}^{\text{rep}} = -\nabla V^e$, where V^e is one of the two interaction potentials of (9). In our implementation, we simply replace

∇ by \mathcal{D}_ℓ and interpolate gradient values on the staggered grid to determine the total force on each particle. Numerical evaluation showed that replacing ∇ by \mathcal{D}_ℓ in expression (10) or (11), which were derived following rules for the continuum gradient, shifts the balance between attractive and repulsive forces via an effective scaling of \mathbf{F}^{rep} . This small but significant shift of the phase boundaries was identified by a direct comparison to both the selected implementation and the phase boundaries determined by mean-field theory.

To investigate and minimize the role of discrete (gradient) operators completely, we may also compare the reference mean-field binodal to the one that is numerically obtained by a Monte Carlo (MC) approach. In this approach, we determine the (fluctuating) density field that optimizes the density-dependent mean-field free energy (1) with a term for the translational entropy included. As usual in MC, a random move (of maximum size r_{\max}) is performed on a randomly selected particle in each step, which is accepted or rejected based on a criterion that involves the free energy of the updated projected particle distribution. As such, the MC results provide insight into the validity of our implementation and into the significance of artifacts that appear due to the chosen projection scheme. We have considered different r_{\max} and two starting conditions—a fully mixed state and the final phase-separated state of the hPF-MD simulations—to evaluate key dependencies and show only data for one set. Each MC run comprises roughly $4 \cdot 10^8$ MC steps.

E. Simulation setup

1. Microscopic representation

It is good to realize that one may select any molecular representation and any system composition in the hPF-MD approach, albeit that a continuum representation is not equally valid for all resolutions. For the current purpose of computationally analyzing a liquid–vapor coexistence, we concentrate on a one-component system, i.e., a system containing only single particles or beads, which is the standard coarse grained (CG) description for a solvent. Each of these CG particles usually represents a small number of solvent molecules. In the Martini method, for instance, CG water particles represent four H₂O molecules. We note that, in standard conditions, liquid water contains about 33 molecules per a unit volume of 1 nm³, while an ideal gas has about 0.027 molecules in the same volume.

2. Dimensionless units

It is convenient, but by no means necessary, to report numerical results in physically sensible units. We therefore scale lengths and time as $\tilde{r} = r/r_0$ and $\tilde{t} = t/t_0$, with $r_0 = 1$ nm and $t_0 = 1$ ps, and consequently velocities as $\tilde{v} = v/v_0$ with $v_0 = 1$ m/s. Temperature and mass are given as $\tilde{T} = T/T_0$, with $T_0 = 1$ K, and $\tilde{m} = m/m_0$, with $m_0 = 1$ amu, while energy is in kJ (=1000 kg m²/s²). All simulations start from a Maxwell–Boltzmann distribution for the particle velocities at a given (kinetic) temperature \tilde{T} with an average kinetic energy,

$$\frac{1}{2} \tilde{m} \langle |\tilde{\mathbf{v}}_i|^2 \rangle = \frac{3}{2} \alpha \tilde{T}, \quad (17)$$

with $\alpha = k_B T_0 / m_0 v_0^2 = 0.00831$. The configurational temperature is sometimes advocated as a better measure,²⁰ but it is based on the gradient and Laplacians of the interaction potentials, so we rely on the standard procedure of monitoring the kinetic temperature instead. In our case, the phase behavior should be insensitive to the simulation temperature, which only scales time, and indeed, we find fully matching coexistence curves at $T = 100$ K and 298 K for a system considered with Carnahan–Starling (CS) for $\tilde{v} = 1/8$ and $\tilde{\rho}_0 = 2.92$.

3. Simulation settings

The grid spacing ℓ should be larger than the effective particle radius (which is $\sigma = 0.47$ nm for Martini) to make physical sense, but also small enough to keep sufficient spatial resolution (our default value is $\ell = 1$ nm). As a special note, we again mention that the choice of ℓ is irrelevant for single particle systems, since they carry no explicit length scale. Initially, all n particles are placed in a volume $V = L_x \times L_y \times L_z$ with periodic boundary conditions. For all calculations of phase coexistence, a rectangular simulation volume with $L_x = 8\ell$, $L_y = 8\ell$, and $L_z = 42\ell$ was chosen. Unless mentioned otherwise, particles are initially placed to occupy only half of the total volume.

The restricted x - and y -dimensions of the simulation volume may not allow us to study particular interfacial properties, but they are sufficient for the determination of the coexistence values of the (fractional) densities f_v and f_ℓ in the liquid and vapor phases, which is our main goal. Updates of the “slow” field variables are usually performed only every tenth MD steps or even less frequent,¹⁴ but, for this study, we performed field updates every MD time step for consistency. This setup means that our density and potential fields are instantaneous quantities. Moreover, although we are primarily interested in thermodynamic (equilibrium) properties, we used the recently developed Multi Particle Collision Dynamics (MPCD) extension of hPF-MD that accounts for momentum transfer¹⁷ and has been shown to accelerate phase separation. Owing to the selected phase-separated starting state and the enhanced MPCD kinetics, we may restrict ourselves to relatively short trajectories of 30 000 time steps, with the first 25 000 steps serving the purpose of equilibration and thermalization. During simulation, we monitor the evolution of $W[\rho]$ to check convergence. Subsequently, stored particle positions for 50 instances collected at equal intervals during the last 5000 time steps were used to determine particle profiles in a post-processing step. Instead of projected densities, we consider particle profiles obtained by binning with a bin width of 0.05 nm along the longest z -direction, i.e., perpendicular to the liquid–vapor interface, where we average over x and y coordinates and scale by a factor $\tilde{\rho}_0/v$ to obtain $f(z)$.

When $\tilde{\chi}$ is below the critical value $\tilde{\chi}_c$, single-component systems will phase separate into particle-rich (liquid) and particle-poor (vapor) regions when performing nVT -simulations with an excluded volume term (7). As in experiments, the average fraction $f = \tilde{v}$ of the system associated with the homogeneous situation should be chosen in an interval between the two coexistence curves, i.e., $f_v < \tilde{v} < f_\ell$, for the system to exhibit phase separation. It is also clear that, as in experiments, the volume of the liquid and vapor regions is tuned by the choice of the scaling parameter \tilde{v} . Here, we will consider two values of \tilde{v} : $\tilde{v} = 1/4$ and $\tilde{v} = 1/8$.

III. RESULTS AND DISCUSSION

A. Mean-field phase diagram

To obtain the reference values for the new hybrid model, we first determine liquid–vapor, mean-field phase diagrams for a one-component field description, considering both the Cell Model and the Carnahan–Starling expression for the excluded volume interactions (7).

The usual mean-field expression for the (grand) free energy as a function of the (number) density ρ is given by

$$\frac{\Omega(\rho)}{V} \equiv g(\rho) = f_{\text{hs}}(\rho) + \frac{\chi}{2} \rho^2 - \mu \rho, \quad (18)$$

where $f_{\text{hs}}(\rho)$ is the free energy (per volume) of a hard-sphere reference system and μ is the chemical potential that has to be chosen such that a liquid and vapor phase coexist, i.e., $\mu = \mu_{\text{coex}}$. The usual interaction parameter χ can be expressed in terms of the attractive interactions between molecules,

$$\chi = \int d\vec{r}_{12} U_{\text{att}}(r). \quad (19)$$

For $f_{\text{hs}}(\rho)$, we shall specifically consider both the Carnahan–Starling expression

$$f_{\text{hs}}^{\text{CS}}(\rho) = k_B T \rho \ln(\rho) + k_B T \rho \frac{(4\eta - 3\eta^2)}{(1 - \eta)^2} \quad (20)$$

and the Cell Model expression

$$f_{\text{hs}}^{\text{Cell}}(\rho) = k_B T \rho \ln(\rho) - 3 k_B T \rho \ln(1 - \eta^{1/3}), \quad (21)$$

with the usual volume fraction $\eta = (\pi/6)\rho\sigma^3$ for a molecular diameter σ . More generally, the volume fraction can be defined as $\eta \equiv v\rho$, in line with the simulations. The free energy in terms of the volume fraction can be recast in a form such that the dependence on v vanishes. For instance, for the Carnahan–Starling expression, the free energy can be rewritten as

$$\frac{\Omega v}{k_B T V} \equiv g(\eta) = \eta \ln(\eta) + \eta^2 \frac{(4 - 3\eta)}{(1 - \eta)^2} + \frac{\tilde{\chi}}{2} \eta^2 - \tilde{\mu} \eta, \quad (22)$$

where again $\tilde{\chi} \equiv \chi/(k_B T v)$ is the dimensionless parameter.

The procedure to determine the phase diagram from the expression for $g(\eta)$ in (22) (or any similar expression) is outlined in the [supplementary material](#). The resulting phase diagram is shown in [Fig. 2](#).

Also shown in [Fig. 2](#) are MD simulation results for a Lennard–Jones system. In order to compare with the MD results, we have set $v = (\pi/6)\sigma^3$ and $\tilde{\chi} = -26.394/T^*$, where $T^* \equiv k_B T/\epsilon$ is the usual Lennard–Jones reduced temperature. The numerical factor in the expression for $\tilde{\chi}$ is determined by inserting the attractive part of the Lennard–Jones potential used by Watanabe *et al.*²¹ into (19). In [Fig. 3](#), the same results are shown in terms of the usual reduced Lennard–Jones units.

B. Monte Carlo route to the mean-field phase diagram for CS

Before analyzing the compressible hPF-MD approach, we shortly review an alternative free energy minimization method for

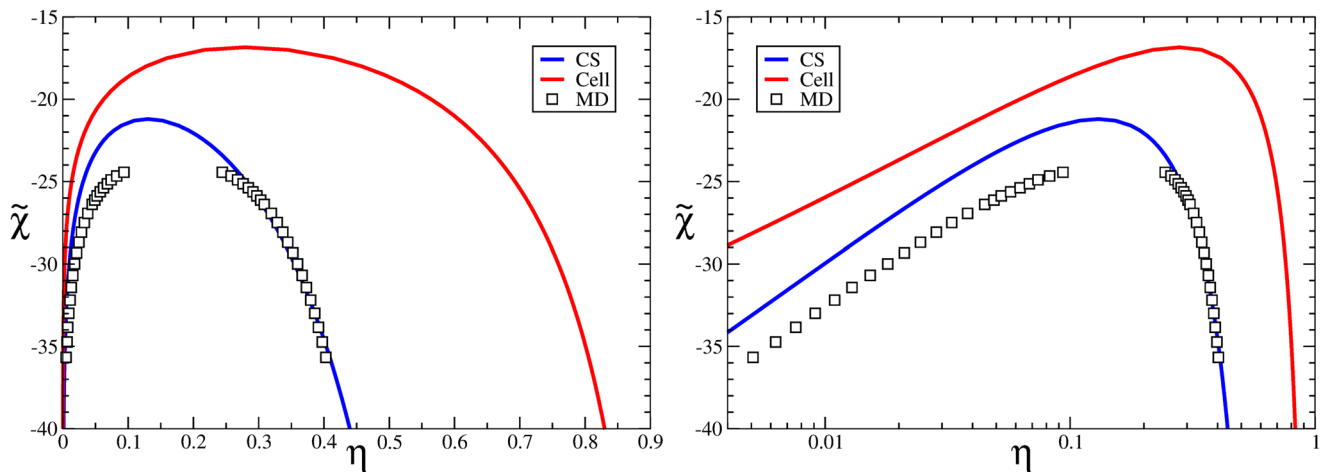


FIG. 2. (Left) Mean-field liquid–vapor phase diagram as a function of the interaction parameter $\tilde{\chi}$ and volume fraction η for the Carnahan–Starling and cell model expression for the hard-sphere free energy. The square symbols are MD simulation results from Watanabe *et al.*²¹ (Right) The same results using a logarithmic scale for η .

fluctuating fields, which are obtained as the projection of moving particle ensembles in MC. For simplicity, we focus on the Carnahan–Starling model. This approach thus complements the mean-field treatment for CS in Subsection III A, concentrating on the validity of the implementation and on the performance of the considered projection schemes. By ruling out the finite difference operators and interpolation schemes altogether, these results can also be employed to offset hPF-MD results in Subsections III C and III D.

In each MC step, a randomly selected particle is displaced over a random direction by a step size that is upper bounded by r_{\max} . This move is rejected or accepted based on the standard MC criterion that

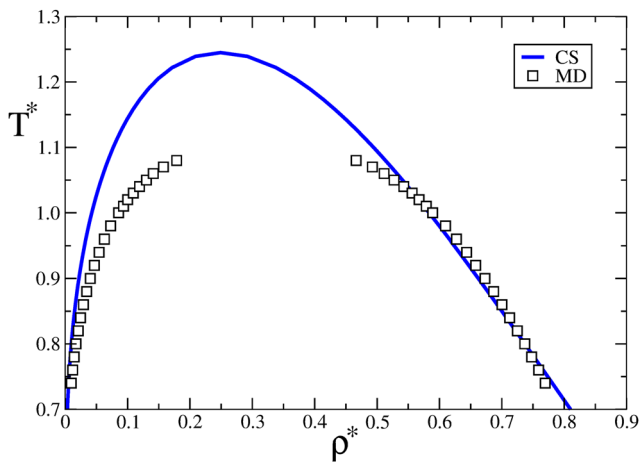


FIG. 3. Mean-field liquid–vapor phase diagram as a function of reduced temperature $T^* = k_B T / \epsilon$ and density $\rho^* = \rho \sigma^3$ for the Carnahan–Starling expression for the hard-sphere free energy. The square symbols are MD simulation results from Watanabe *et al.*²¹

considers the difference in free energy for the old and new projected fields, which can be efficiently calculated since density fields only change in a few lattice positions. On average, we performed about 8×10^8 steps for different ρ_0 with a dimensionless r_{\max} between $r_{\max} = 0.1 - 0.5\ell$. Although MC results do not depend on such algorithmic parameters, selecting proper values for the step size and the number of MC steps, as well as the average particle density, is important in our case.

Here, we draw inspiration from two observations. While the considered free energy functional lacks a square-gradient term that promotes a reduction in the total surface area, surface tension is included via the non-locality of the interactions, which can be tuned by the particle-to-field projection. For the considered number of MC steps, we nevertheless observe that the high- and low-density phases do not grow beyond the scale of a few cells, which suggests that this tension is low. Desiring narrow density distributions, we therefore selected a small r_{\max} . Moreover, the low-density phase will install a requirement for the actual number of particles per grid cell that suggests a choice for a higher ρ_0 . Numerically, we indeed found that density distributions become better defined with decreasing r_{\max} and increased ρ_0 ; we focused our analysis on the results with the narrowest distributions.

As expected, when starting from a homogeneous particle distribution, phase separation into vapor and liquid nuclei is quick, but the growth of these small nuclei into larger domains is significantly impeded. Lacking a well-defined, extended liquid–vapor interface, we determined f_v and f_ℓ from the density distribution by fitting the two peaks to Gaussians. For the projection using the Gaussian kernel, which gives rise to a broader density distribution due to its longer-ranged interactions, we started from the final snapshot of the hPF-MD simulations for the same $\tilde{\chi}$. Here, we report only the mean and standard deviations of these Gaussian fits.

Concentrating on the phase behavior determined by MC (see Figs. 4 and 5), it is clear that the results for both projection schemes agree very well with the mean-field binodal curves. Two types of

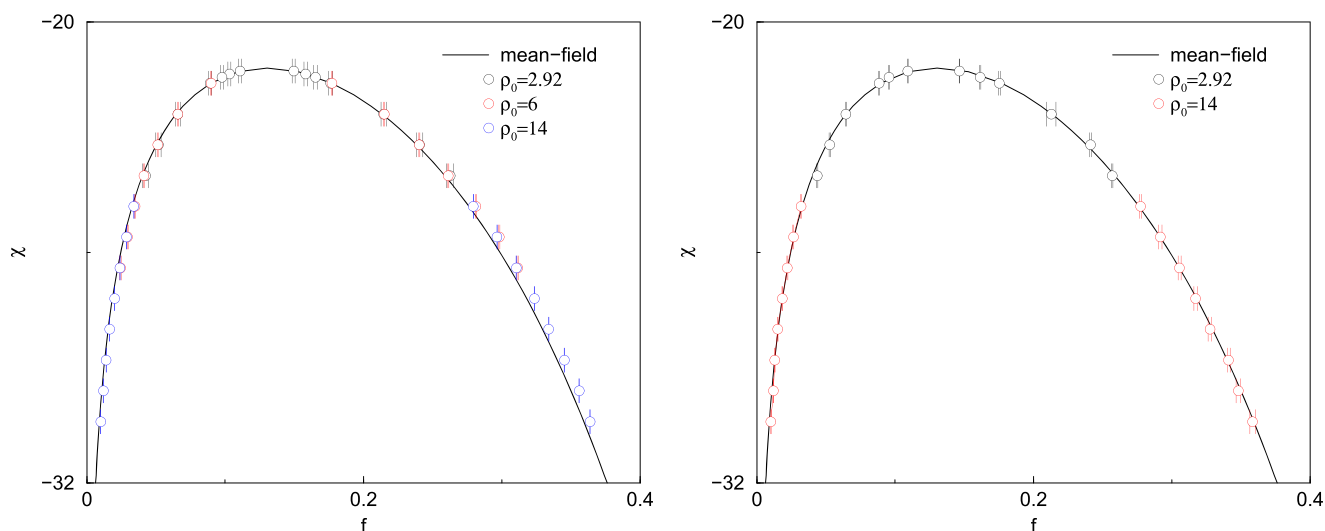


FIG. 4. Phase diagrams for the Carnahan–Starling model determined from the Monte Carlo (MC) treatment for two different projection schemes: CIC (left) and the Gaussian kernel (right). Simulations were performed at different particle densities, with $n = 7836$ ($\bar{\rho}_0 = 2.92$), $n = 16\,896$ ($\bar{\rho}_0 = 6$), and $n = 37\,632$ particles ($\bar{\rho}_0 = 14$) occupying a volume $\bar{V} = 8 \times 8 \times 42$. The mean-field phase diagram for the Carnahan–Starling model is added as a reference.

deviations from the mean-field prediction can be observed (see Fig. 6 for details): (1) for the cloud-in-cell projection scheme, the f_ℓ shows a constant relative offset to the reference values, while the liquid fractions for the Gaussian kernel show perfect agreement within numerical precision, especially for the largest average particle density considered, and (2) as expected, the vapor fraction f_v determined by simulation is somewhat sensitive to the issue of representability for both projection schemes. An equivalent conclusion is that the vapor phase is more sensitive to fluctuations. Yet, also here, the Gaussian

kernel projection provides the best results, breaking down only when the reference fractions correspond to a very low number of particles per grid cell.

In addition to the phase diagrams, we also performed MC for a system at $\bar{\chi} = -16$, i.e., above the critical $\bar{\chi}_c$ or in a single (mixed) phase. In a mean-field description, such a homogeneous situation should not carry any structure, meaning that $\rho(\mathbf{r}) = \rho_0$ at each grid node. The density field obtained from MC, however, will fluctuate over time, but if we average out this fluctuating part by averaging

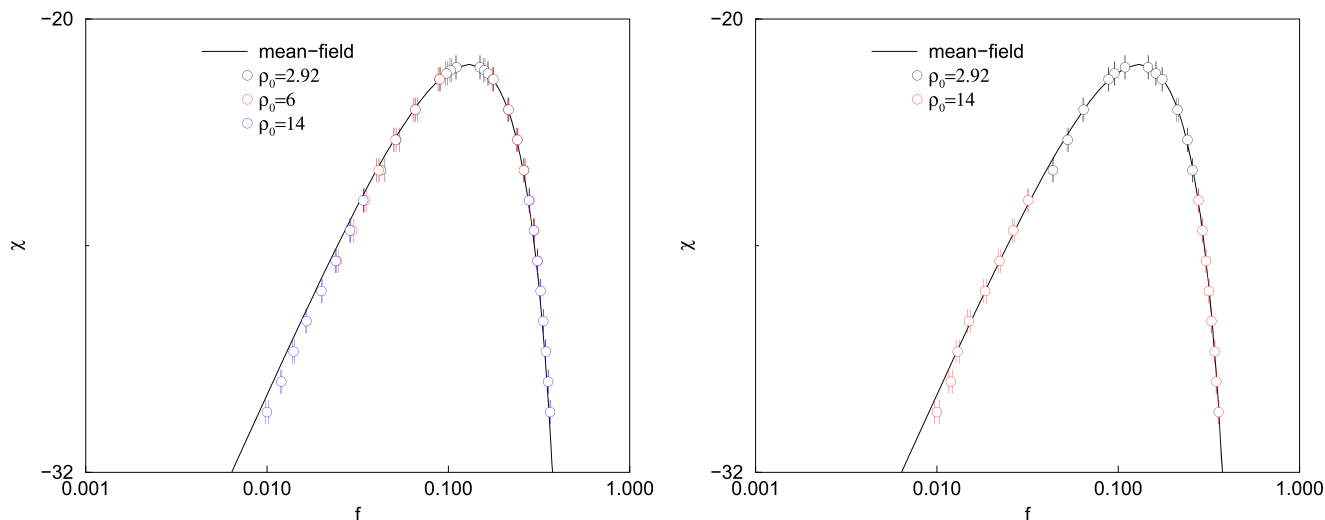


FIG. 5. Data of Fig. 4, but on a log-linear scale for closer inspection of the vapor branch.

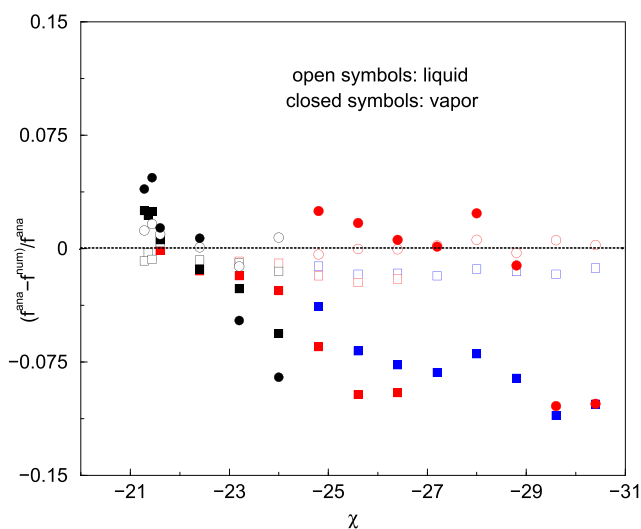


FIG. 6. Relative differences $(f^{\text{ana}} - f^{\text{num}})/f^{\text{ana}}$ between the mean-field value f^{ana} and the numerically determined average value f^{num} for the considered $\tilde{\chi}$. Open symbols denote the fraction f_ℓ in the liquid phase, and closed symbols denote the corresponding f_v of the vapor phase. The two projection schemes are distinguished by different symbols: \square (CIC) and \circ (Gaussian kernel), while colors reflect the particle densities considered (see Fig. 4 for the color scheme).

over a long time (in our case: many MC moves), the radial distribution function (RDF) should approach unity for all radial distances. In other words, hypothetically, the (averaged) MC result should be equivalent to a homogeneous field on the field level and to an ideal gas on the particle level.

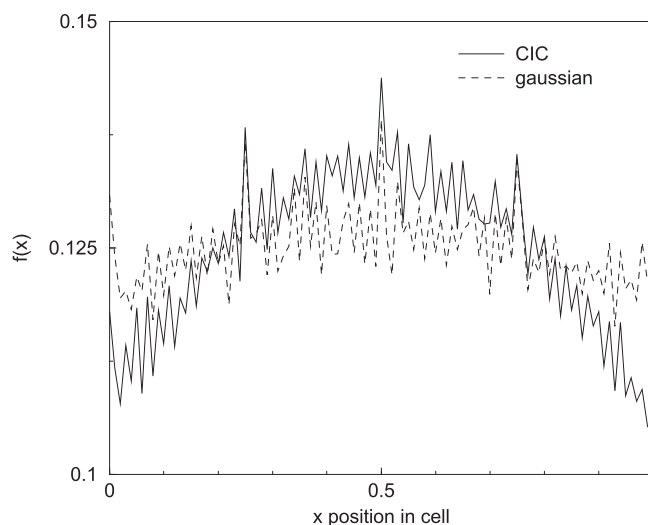
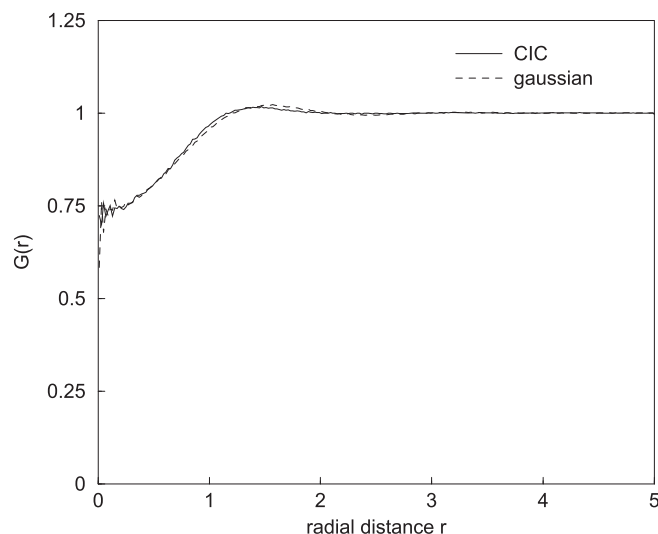


FIG. 7. Radial distribution functions $G(r)$ vs radial distance r (left) and cell profiles $f(x)$ vs x direction (right) for the two projection methods: linear interpolation (CIC, solid line) and Gaussian kernel (Gaussian, dashed line). Simulations involved 1.5×10^8 MC moves ($r_{\text{max}} = 1.5\ell$) and a $\tilde{V} = 10 \times 10 \times 10$ volume, for $\tilde{\chi} = -16$, with $\tilde{v} = 1/8$ and $\tilde{\rho}_0 = 2.92$ ($n = 2915$ particles). Cell profiles were obtained as histograms, averaging over cells and 3×10^4 MC steps (each separated by 2915 steps) at the end of the MC trajectory by binning with a bin width of 0.01.

Figure 7 shows actual RDFs (left) obtained from MC results for both projection methods considered. We find that the RDFs are very similar and show a weak correlation hole at the closest distances. Concentrating on the particle profiles along the x -direction in the computational cell [see Fig. 7 (right)], we see that roughly the same RDF corresponds to a parabolic particle-in-cell distribution for the CIC projection scheme and a much more evenly spread distribution for the Gaussian kernel projection. As such, they illustrate distinct features of the two projection schemes. For completeness, we note that the particle-in-cell profiles along the other Cartesian directions are equivalent. Moreover, we find that the correlation hole increasingly fills in and that the particle-in-cell distribution increasingly flattens for an increased choice of ρ_0 (results not shown), as expected.

Overall, we conclude that the MC results for a Gaussian kernel agree within numerical precision with the mean-field reference curves and that the cloud-in-cell projection also does a proper job. Since the CIC projection is more efficient than the Gaussian kernel projection, by a factor of 8 (8 vs 64 grid points for each particle), a basic investigation of dependencies, i.e., properties that are insensitive to the selected projection scheme, is performed for hPF-MD with the standard CIC projection.

C. Properties of the hybrid CS model

The comparison of Fig. 2 clearly shows that the mean-field Carnahan–Starling (CS) model is more accurate than the Cell Model (CM) in reproducing the phase behavior of the Lennard-Jones particle system, which, in turn, has been shown to match the phase behavior of neon in the vicinity of the critical point. For clarity of presentation, we therefore limit our investigation of the new compressible hPF-MD method to the CS model in this study, just like in

Subsection III B. We refer to the [supplementary material](#) for a few exemplary results for the cell model. Our standard particle density $\bar{\rho}_0 = 2.92$ particles per grid cell.

Particle fractions in the vapor and liquid phases, f_v and f_ℓ , are usually determined by fitting the simulated liquid–vapor interface profile to the functional form imposed by Maxwell–van der Waals theory,²²

$$f(z) = f_v + \frac{f_\ell - f_v}{2} \left(\tanh\left(\frac{z - z_0}{\lambda}\right) + 1 \right), \quad (23)$$

where z_0 and λ are the position and thickness of the interface, respectively. Interfacial profiles are obtained from time-averaging and binning of simulated particle distributions instead of particle concentration fields. After all, the compressible hPF-MD scheme is particle-based. We note however that, close to the critical point, long-range correlations give rise to composition fluctuations that render the determination of tanh-profiles far from ambiguous. The same can be said for systems far away from the critical point, i.e., at higher liquid phase density, where the liquid–vapor interface is found to show the oscillatory behavior that has been predicted and discussed before.^{8,23,24} Especially for liquid domains of restricted dimensions (see the previous discussion about its relation to the choice of \bar{v}), one may wonder how these oscillations affect the fitting procedure for f_ℓ . To be concise, we alternatively determined f_v and f_ℓ from the average bulk densities in the liquid and vapor phases. Direct comparison shows that both procedures give rise to very similar results.

First, we consider the same homogeneous system ($\tilde{\chi} = -16$) that was previously considered with MC (see Fig. 7 for a reference). Figure 8 shows the RDFs (left) and particle-in-cell distributions (right) obtained by simulating this system using compressible

hPF-MD for both projection methods considered. The results are clearly well in line with the expectations expressed in the discussion in Subsection III B. Close inspection reveals that the Gaussian kernel projection gives rise to a slightly smoother RDF, which is closer to unity for all radial distances.

Next, we discuss exemplary density profiles for a few selected $\tilde{\chi} = \chi/(k_B T v) < \tilde{\chi}_c$ (see Figs. 9–11) and focus on the effect of smoothing as well as the choice of the particle volume v and the grid spacing ℓ in the phase separation characteristics. Starting with smoothing (see Fig. 9), we observe that the interfacial particle profiles for the systems closest to the critical values $\tilde{\chi}_c$ agree quite well with the grid-restricted values of the smoothed continuum representation, as well as the tanh functional form (23). For deeper quenches or more negative $\tilde{\chi}$, however, profiles relating to the two representations are still very similar in terms of average properties, but they start to deviate in detail. We observe distinct oscillatory behavior, i.e., particle enrichment close to the liquid–vapor interface followed by depletion in the liquid phase, the amplitude of which increases with decreasing $\tilde{\chi}$. Previously, such excluded volume oscillations have been attributed to nonlocal correlations that are not fully captured by short-ranged pair correlations in LJ fluids.⁸ They can be seen as a realistic physical phenomenon, albeit that they are usually considerably damped by capillary wave fluctuations of the interface.⁸

An aspect worth mentioning is that while the thermodynamic laws underlying phase-equilibria in hPF simulations and mean-field SCF are the same, the EOS and density dependence of chemical potential in hPF differ from the mean-field SCF because of fluctuations and local correlation effects that the mean-field SCF neglects. Moreover, in hPF-MD, equilibrium is reached via a (dynamic) balance of particle forces stemming from attractive and repulsive

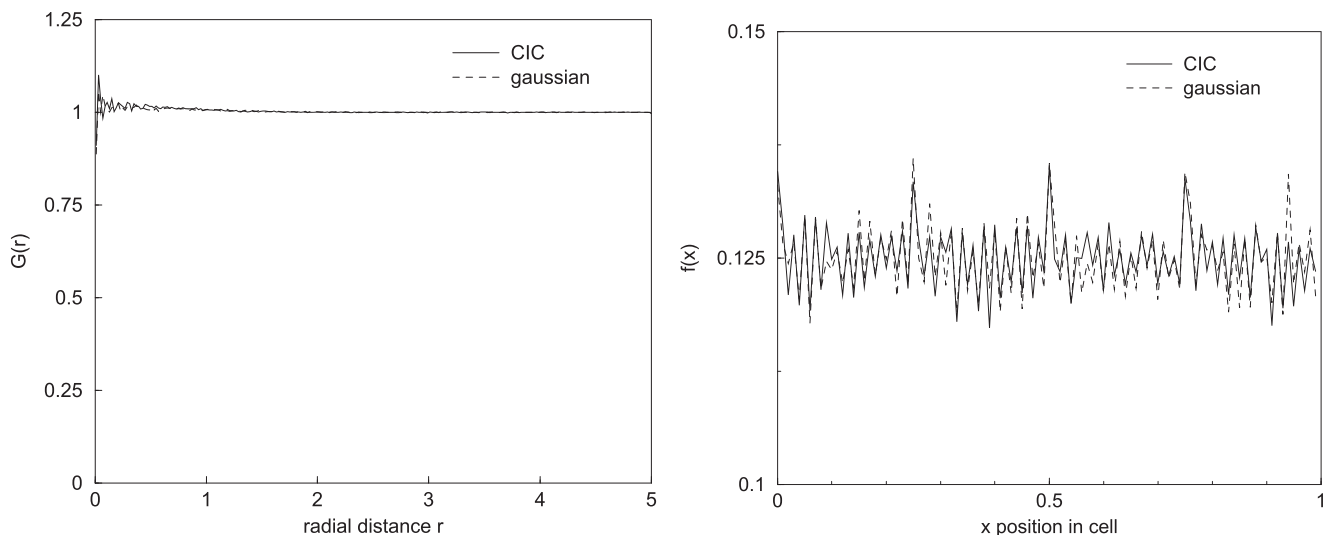


FIG. 8. Radial distribution functions $G(r)$ vs radial distance r (left) and cell profiles $f(x)$ vs x direction (right) for the two projection methods: linear interpolation (CIC, solid line) and Gaussian kernel (Gaussian, dashed line). The compressible hPF-MD simulations considered 5×10^4 time steps in total and a $\bar{V} = 10 \times 10 \times 10$ volume, for $\tilde{\chi} = -16$, with $\bar{v} = 1/8$ and $\bar{\rho}_0 = 2.92$ ($n = 2915$ particles). Cell profiles were obtained as histograms, averaging over cells and the last 3×10^4 MD steps by binning with a bin width of 0.01.

Carnahan–Starling

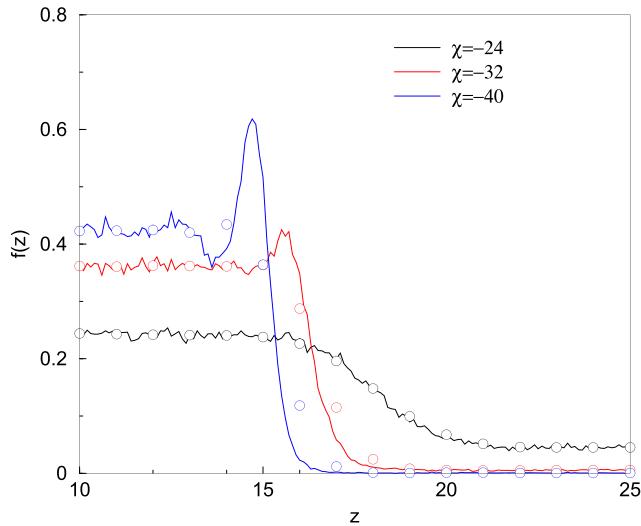


FIG. 9. Density profiles $f(z)$ (solid lines) and grid values (open circles) as a function of the height z (in nm) determined from compressible hPF-MD simulations for different values of $\bar{\chi}$ with $\bar{v} = 1/8$ and $\bar{\rho}_0 = 2.92$. Profiles are obtained as histograms by binning with a bin width of 0.1 nm and averaged over time as well as x and y directions.

Carnahan–Starling

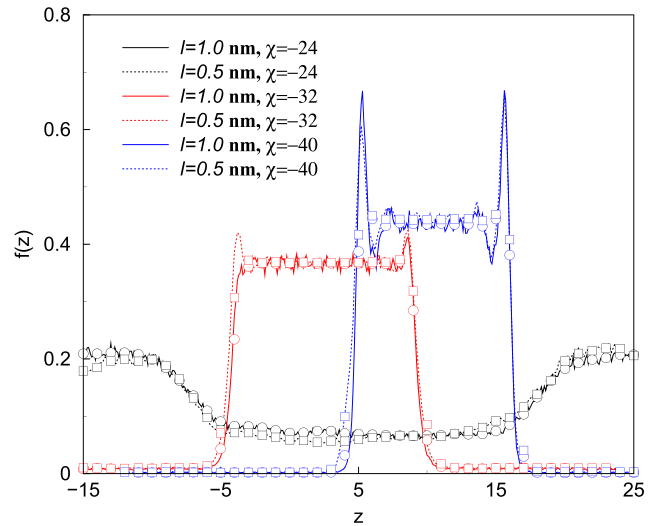


FIG. 11. Density profiles $f(z)$ (solid lines) and grid values (open symbols) as a function of the height z (in units of ℓ) determined from compressible hPF-MD simulations for different values of $\bar{\chi}$ with $\ell = 1$ nm (solid line with circles) and $\ell = 0.5$ nm (dotted line with squares). In some case, results have been shifted along the horizontal direction for clarity. Results are obtained for $\bar{v} = 1/8$ and $\bar{\rho}_0 = 2.92$.

interactions, whereas in the mean-field SCF, the chemical potentials in the liquid and vapor phases have to match exactly. In fact, each particle in the MD-SCF can be seen subjected to an external field generated by the particle ensemble. By determining

Carnahan–Starling

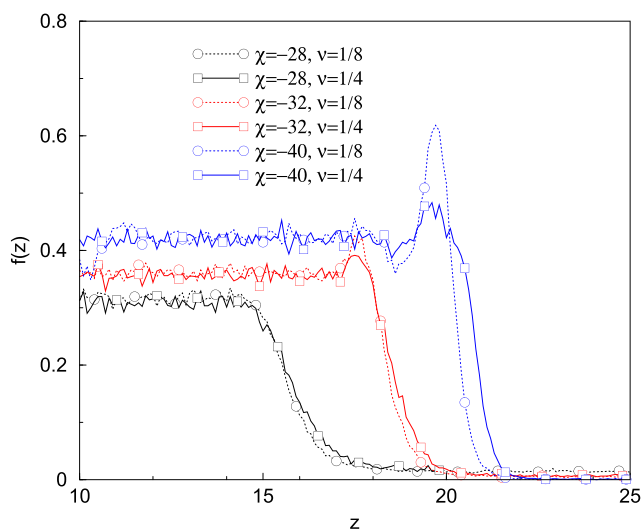


FIG. 10. Density profiles $f(z)$ (solid lines) and grid values (open circles) as a function of the height z (in nm) determined from compressible hPF-MD simulations for different values of $\bar{\chi}$ with $\bar{v} = 1/4$ (solid line) and $\bar{v} = 1/8$ (dotted line). Results are obtained for $\bar{\rho}_0 = 2.92$.

particle forces from (excess chemical) potentials of SCF via a sequential particle-to-field and field-to-particle projection, we neglect higher frequency fluctuations in the underlying particle density. In particular, although the average density over a grid cell is indeed found to match the field-based density values quite well, these fluctuations are lost in the smoothed field representations (see Fig. 9). Consequently, this fluctuating component is also absent in the forces that each of the particles experience, and we may thus conclude that the force density is also smoothed. Particularly, when the potential $\mu(f)$ is very sensitive to minute variations in f , which is the case for larger f in the CS model, this may have an observable effect on the detailed force balance. Such an issue is complementary to the issue of representability, which requires that there are sufficient particles per grid cell or sufficiently small and non-empty grid cells to warrant a smooth projected ρ . Since these two conditions are only satisfied for minute grid cells that are all occupied by at least a single particle, i.e., incompatible with liquid–vapor coexistence in most practical setups, the phase behavior for the hybrid model may always slightly deviate from that of the mean-field SCF even when the fluctuations are averaged out of the hPF-MD results during post-processing.

As analytically predicted, the particle volume v is found to be an independent parameter (see Fig. 10) that sets the volume ratio between the liquid and vapor phases in the simulation volume. Yet, while the liquid and vapor fractions f_ℓ and f_v show no notable dependence on v , the amplitude of the oscillations close to the liquid–vapor interface can be seen to vary. Close inspection reveals that these oscillations, which are present at either side of the liquid–vapor interface, are often not fully symmetric.

Next, we test our observation that a physical length scale is absent in our setup by simulating the same systems for a twice denser grid (i.e., for $\ell = 0.5$ nm, see the results in Fig. 11). For direct comparison, we have used ℓ as the reference length scale for the visualization of profiles instead of the usual $r_0 = 1$ nm. We indeed find good agreement between all results for the two different ℓ , albeit that the interfacial properties vary slightly, which is in line with our earlier findings. Yet, in the absolute sense, the width of the interfacial profile can be seen to scale with ℓ , which highlights the hPF-MD property that the range of the non-bonded interactions varies with the grid spacing. After all, smoothed particle fields are obtained by the projection of particle fractions to neighboring grid points within a certain range,¹⁹ so particle pairs separated by more than that amount of grid points do not interact.

A comparison of results for the same system but an increasing number of particles that is added to the volume (see Fig. 12) highlights the role of the hybridization. Particularly for smaller $\tilde{\rho}_0 < 10$, the discrete particle system is not fully adequate in describing the continuum field variable at equilibrium, which gives rise to a slight mismatch compared to the limiting profile that is increasingly approximated for higher values of ρ_0 . In absolute terms, however, these deviations remain small, particularly when taking into account that the fluctuations in the binned particle profile are roughly of the same magnitude as this mismatch.

The effect of the two considered projection schemes, cloud-in-cell (CIC) and a Gaussian kernel (Gaussian), on the smoothness and interfacial thickness of the profile is shown in Fig. 13. While restricting the interaction range is quite standard, e.g., truncating the LJ potential beyond a certain cutoff is usual in MD, the new aspect of hPF-MD is that the interaction range varies automatically with changing ℓ . The consequence is that not only the total (potential)

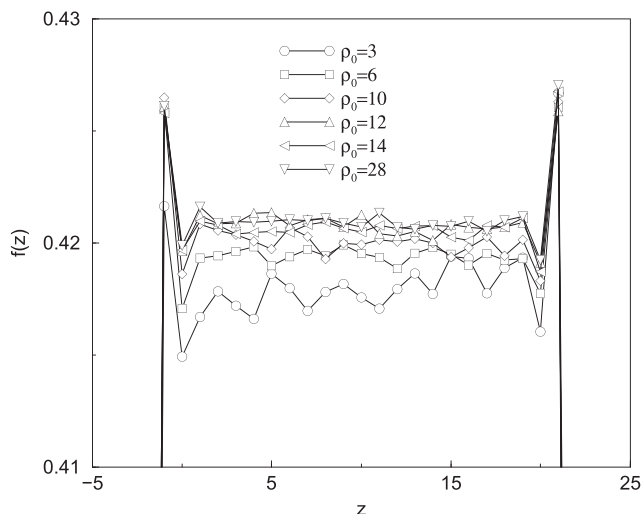


FIG. 12. Density profile grid values (open symbols connected by lines to guide the eye) as a function of the height z (in nm) determined from compressible hPF-MD simulations for different values of $\tilde{\rho}_0$, obtained by varying the number of particles in the simulation volume $\tilde{V} = 8 \times 8 \times 42$ between $n = 8064$ and $n = 75\,264$. Grid values are collected by averaging over the last 50 snapshots of a simulation that considered 20 000 steps in total. Results are obtained for $\tilde{v} = 1/4$ and $\tilde{\chi} = -40$.

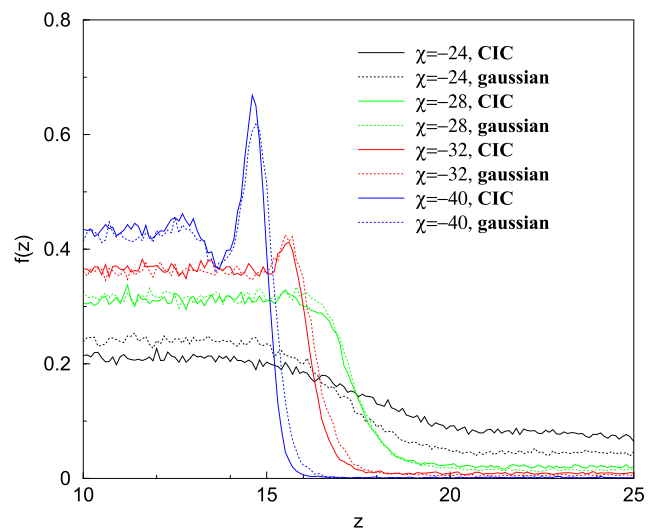


FIG. 13. Density profiles $f(z)$ as a function of the height z (in nm) determined from compressible hPF-MD simulations for different values of $\tilde{\chi}$. Two types of projection schemes are considered: cloud-in-cell (CIC, solid line) and a Gaussian kernel (Gaussian, dotted line). Results are obtained for $\tilde{v} = 1/4$ and $\tilde{\rho}_0 = 2.92$.

energy of a system depends on the selected ℓ but also that simple evaluation of discretization artifacts by systematically varying ℓ is not a viable option. Compared to mean-field SCF on the other hand, where field interactions are entirely localized [see the cohesive term in (3)], the same non-ideal term gives rise to a finite interaction range through the projection algorithm in hPF-MD. This shows that the hPF method truly belongs to a separate class. We set $\ell = 1.0$ nm in the remainder.

D. Phase diagram for the Carnahan–Starling model

The phase diagram (PD) obtained by hPF-MD simulation with the Carnahan–Starling model is shown in Figs. 14–16 for several values of the various parameters, different projection methods, and two different approaches employed to determining liquid and vapor fractions from particle density profiles. Profiles were determined from time-averaging over many instantaneous particle conformations along a fixed trajectory. Figure 14 compares fractions f_v and f_ℓ that are either obtained by fitting the averaged liquid–vapor interface profile to the tanh-form or by determining averaged plateau values in the liquid and vapor regions. Mean-field results have been added as a reference.

We note that this comparison confirms our earlier statement that both approaches used for analysis give rise to very similar results for both projection schemes considered. Only for the strongest interactions or lowest $\tilde{\chi}$ considered, the selected approach makes a difference. In this range, determination of f_v by averaging provides slightly reduced values when compared to tanh fitting, for both projection schemes, and the opposite can be seen for the f_ℓ relating to the cloud-in-cell projection. We note that these findings are easily understood in terms of a mismatch of the actual profile from the imposed functional form, which was, after all, derived from mean-field theory. Fluctuations, which are more pronounced in the dilute

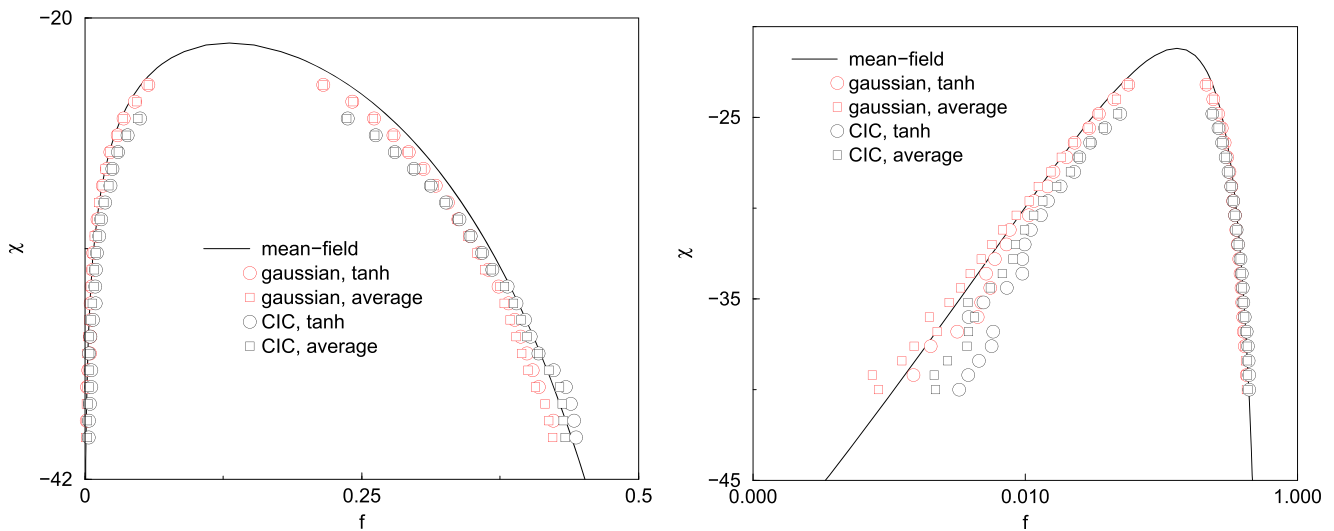


FIG. 14. (Left) Phase diagram for the Carnahan–Starling model determined from compressible hPF-MD simulations. Two projection schemes and two routines for extracting f_v and f_ℓ are considered: the cloud-in-cell (CIC) method or projection based on a Gaussian kernel (Gaussian), and fitting the density profile to a tanh-profile or by calculating the average density in bulk. Simulations were performed for $\tilde{v} = 1/8$ and $\tilde{\rho}_0 = 2.92$ in a volume $\tilde{V} = 8 \times 8 \times 42$. (Right) The same data but on a log-linear scale for closer inspection of the vapor branch. The mean-field phase diagram for the Carnahan–Starling model is added as a reference.

phase, are not included in a mean-field description. In particular, as discussed in some detail before, particle profiles for deeper quenches start to display increasingly distinct oscillatory behavior close to the interface, both in the liquid and vapor phases, the amplitude of which is more pronounced for the cloud-in-cell than the Gaussian kernel projection and the same $\tilde{\chi}$. Clearly, since such features are absent in any mean-field profile, fitting to such a reference will lead

to a small but notable mismatch. We will thus further consider the averaging approach.

Finally, we focus on the hPF-MD results and the role of the grid spacing ℓ and the maximum particle density ρ_0/v . Repeating the earlier argument that our system lacks any distinct length scale, it is good to find that the phase diagram for $\ell = 1.0$ nm and $\ell = 0.5$ nm is consistent over the $\tilde{\chi}$ -range considered (see Fig. 15). Small

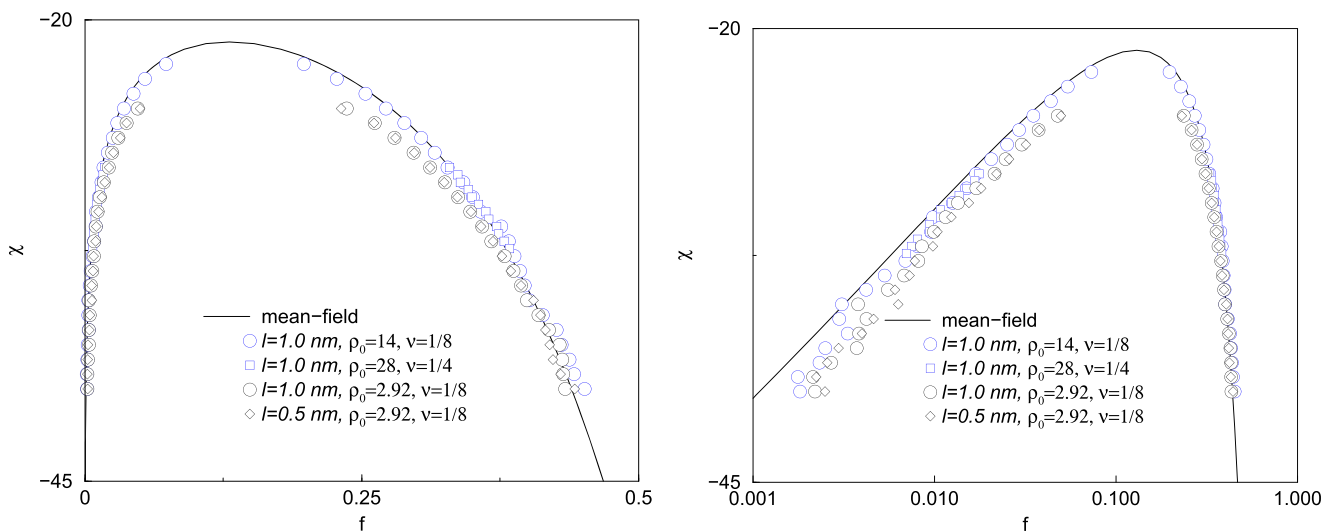


FIG. 15. (Left) Phase diagram for the Carnahan–Starling model determined from the compressible hPF-MD simulations. Simulations were performed using the cloud-in-cell (CIC) projection method and different parameter combinations: $\tilde{v} = 1/4$ or $\tilde{v} = 1/8$, $\ell = 0.5$ nm or $\ell = 1.0$ nm, and $\rho_0/v = 23.36$ or $\rho_0/v = 112$. (Right) The same data but on a log-linear scale for closer inspection of the vapor branch. The mean-field phase diagram for the Carnahan–Starling model is added as a reference.

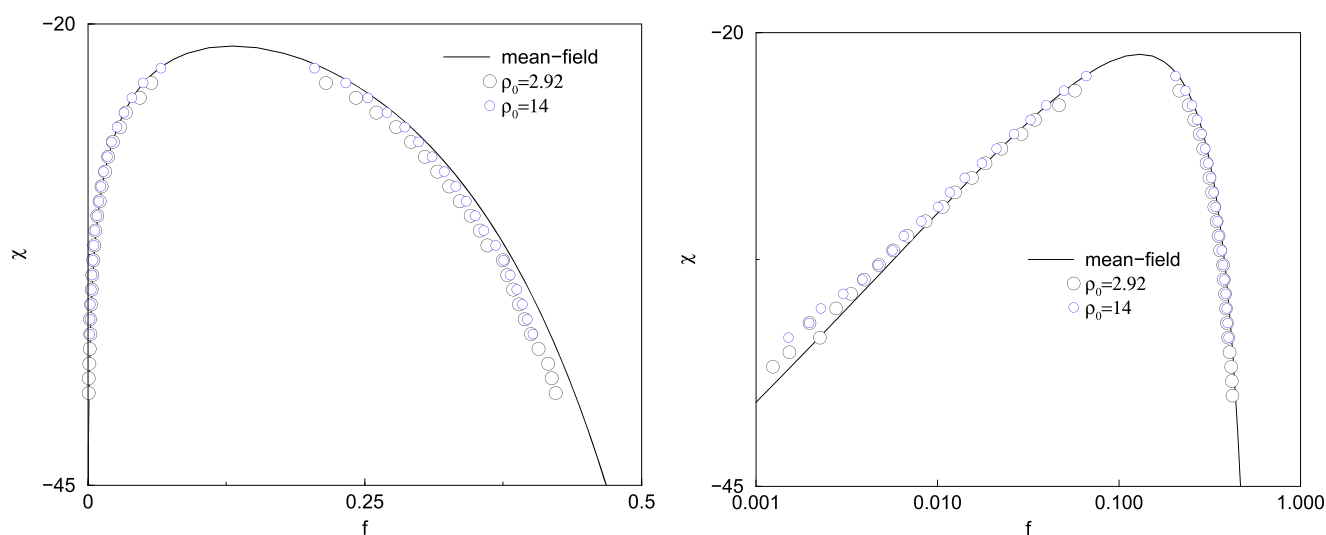


FIG. 16. (Left) Phase diagram for the Carnahan–Starling model determined from the compressible hPF-MD simulations. Simulations were performed using the Gaussian kernel projection method and for two different particle densities $n = 7836$ ($\bar{\rho}_0 = 2.92$) or $n = 37\,632$ particles ($\bar{\rho}_0 = 14$) occupying a volume $\bar{V} = 8 \times 8 \times 42$. (Right) The same data but on a log-linear scale for closer inspection of the vapor branch. The mean-field phase diagram for the Carnahan–Starling model is added as a reference.

mismatches can be seen for deeper quenches where there is a representability issue due to the fact that some of the grid cells in the vapor phase are necessarily devoid of particles. Another issue that may add to the tiny mismatch in this particular case is the size of the simulation volume, which is eight times reduced for $\ell = 0.5$ nm, and the likewise reduced volumes of the liquid and vapor domains, which may play a role in the averaging procedure. As before, the phase behavior can indeed be seen independent of the effective volume v . Results for $\bar{v} = 1/4$ and $\bar{v} = 1/8$, but with the same ρ_0/v , can be seen to match closely. Moreover, the results for increased ρ_0/v are in excellent agreement with the mean-field reference curves with the exception of the lowest $\bar{\chi}$ -values considered, which again suffer from representation issues.

To conclude, we switch to the projection that is based on the Gaussian kernel (see Fig. 16) and only focus on varying the average particle density for $\bar{v} = 1/8$. Somewhat surprisingly, the results for the lowest considered $\bar{\rho}_0 = 2.92$ can be seen to match the vapor branch of the reference binodal equally well as for the higher considered $\bar{\rho}_0$, up to very low $\bar{\chi}$ -values. The surprise is in the expectation that the representation is sufficient up to $f = 1/23.36 = 0.043$ (or $\bar{\chi} = -23.7$ of the reference curve) and $f = 1/112 = 0.0089$ ($\bar{\chi} = -30.5$) for $\bar{\rho}_0 = 2.92$ and $\bar{\rho}_0 = 14$, respectively; below these $\bar{\chi}$ -values, there is less than one particle per grid cell in the vapor phase on average for the considered average densities $\bar{\rho}_0$. As before, close to the critical point, the reference curve is better matched for the higher average density $\bar{\rho}_0 = 14$.

The earlier calculated phase diagram for MD with Lennard–Jones (LJ) interaction potentials was shown to match the experimental phase behavior of neon quite well close to the critical point.²¹ Further away, experimental data were not considered or absent. The accuracy of predicting the experimental phase behavior of a standard test fluid argon was evaluated for a number of

different equations of state,²⁵ including the Carnahan–Starling–van der Waals EOS used in this study. A new EOS, which combines CS for repulsion and Dieterici-type van der Waals attraction, was found to accurately predict the phase behavior for this mono-atomic liquid and, when tested, even for polyatomic systems such as water, albeit with reduced accuracy.

Close to the critical point, a mean-field description fails to describe the actual phase behavior, but it should be noted that also molecular simulations, which are generally based on two-body interaction potentials, are usually less accurate in the regime where multi-body interactions play a more prominent role. In particular, molecular (particle) simulations and the mean-field CS model will generally feature different scaling behavior near criticality, as determined from

$$\Delta f = f_\ell - f_v \propto |1 - \chi/\chi_c|^\beta, \quad (24)$$

with β being the usual critical exponent. For the LJ (particle) system in 3D, with the interaction strength $\bar{\chi}$ replaced by the temperature T^* , a critical exponent $\beta = 0.325$ and a reduced critical temperature $T_c^* = 1.1$ were previously reported.²¹ For mean-field descriptions, the critical exponent $\beta_{\text{MF}} = 0.5$ is independent of the dimensionality of the system. The small mismatch that is consistently observed between the mean-field SCF and hPF-MD results may thus well be due to the conceptual difference between the two methods, in particular how fluctuations and the entropic contributions are included.

To test this suggestion, it would be worthwhile to determine the critical exponent $\beta_{\text{hPF-MD}}$ for our new hybrid approach. To our knowledge, this was not previously considered, albeit that most hPF developers are aware that the phase behavior will differ from its mean-field counterpart. Yet, in order to do so, we should estimate $\bar{\chi}_c$ for all different setups at hand, since the results in Fig. 16 clearly

suggest that the (apparent) critical value may vary with the average particle density ρ_0 . Here, we use a very simple approach, and we postpone a more precise determination of $\tilde{\chi}_c$ using a procedure like the one developed by Binder²⁶ to the future. In particular, our approach exploits the finding that the scaling behavior for LJ and SCF is sustained further away from the critical point, as exemplified by the results of both methods in Fig. 17. To this aim, we determined the apparent critical value for both considered systems from the best fit of the relation (24) with a single exponent β for the whole considered $\tilde{\chi}$ range. Tested $\tilde{\chi}_c$ varied between the mean-field value $\tilde{\chi}_c = -21.2$ and the closest $\tilde{\chi}$ for which phase separation was observed by simulation, with $|\Delta\tilde{\chi}| = 0.1$. This procedure (intermediate results not shown) gives rise to the best fits $\tilde{\chi}_c = -22.3$ for $\tilde{\rho}_0 = 2.92$ and $\tilde{\chi}_c = -21.8$ for $\tilde{\rho}_0 = 14$ (see the additional datasets in Fig. 17).

Two observations suggest that the results of our crude procedure are consistent. First, as expected, the apparent critical value estimated for the more dense system ($\tilde{\rho}_0 = 14$) is closer to the mean-field $\tilde{\chi}_c$ than for the more dilute system ($\tilde{\rho}_0 = 2.92$). Second, and required for results obtained by the same method, we may conclude from the overlapping straight lines for different ρ_0 in the log–log plot that the critical exponents are the same. We thus conclude that the critical exponent for hPF-MD is indeed in rather good agreement with β_{LJ} , i.e., the critical exponent for a Lagrangian particle-based model. This finding illustrates that hPF-MD and mean-field SCF indeed belong to a different class.

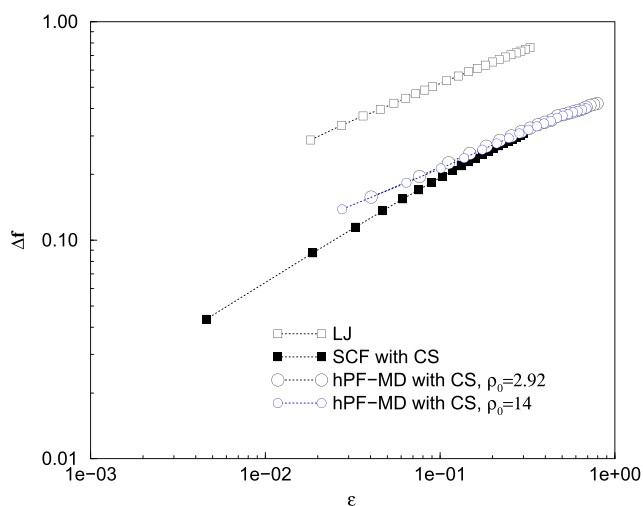


FIG. 17. The liquid–vapor density difference Δf as a function of the reduced interaction strength $\epsilon = |1 - \chi/\chi_c|$ for the reference case (mean-field SCF) and the new hPF-MD simulations for the Carnahan–Starling model and for two particle densities $\tilde{\rho}_0 = 2.92$ and $\tilde{\rho}_0 = 14$. The color scheme of Fig. 16 has been adopted to represent the hPF-MD simulation data. The Lennard-Jones MD simulation results (LJ) of Watanabe *et al.*²¹ for the equivalent order parameter and reduced temperature have been added to this plot as an additional reference. The critical exponents for the reference cases have been previously determined as $\beta = 0.325$ (LJ) and $\beta = 0.5$ (mean-field SCF) and are provided by the slope of the dotted lines that connect data points in this log–log plot. These lines have been added to guide the eye.

IV. CONCLUSIONS

We have established a direct connection between an equation of state (EOS) of choice—in our case, the ones associated with the Cell Model for polymers and the Carnahan–Starling model for hard spheres, which both contain the higher order terms in the density that are needed for a van der Waals loop—and an existing hPF-MD method for particle-field molecular dynamics. In this manner, we extend the applicability of hPF-MD beyond (almost) incompressible systems. Although various systems can be described in the incompressible limit, e.g., liquid solvents and (block co)polymer mixtures, exceptions are, in fact, quite common in reality. Prime examples are cases where crystallization starts in part of a system, e.g., for a liquid-to-gel transition in lipid membranes, or structures that develop while the solvent evaporates, like in (block co-)polymer thin films. In such situations, the standard computational methodology at the mesoscale is known to be handicapped, and a natural desire for treatments that are more physically appropriate arises. Here, we have established a method that is capable of addressing such systems in an efficient fashion.

We have primarily focused on the incorporation of the Carnahan–Starling EOS into the hPF-MD framework, since the results for a simple liquid are more consistent with the earlier determined phase diagram for a Lennard-Jones liquid. We note that it may come as a bit of a surprise that a model for hard spheres can represent “soft” interactions, but our results speak for themselves. We considered both the interfacial profile for increasingly negative dimensionless mean-field interaction strength $\tilde{\chi} = \chi/(k_B T v)$ and the phase behavior in terms of $\tilde{\chi}$ and effective (vapor and liquid) particle fractions f_v and f_ℓ , with $f(\mathbf{r}) = v\rho(\mathbf{r})/(\ell^3\rho_0)$. As a reference, we use a binodal that was determined directly from the associated mean-field free energy by precise numerical analysis. Using Monte Carlo, i.e., including fluctuations but avoiding the use of forces that are determined on the computational grid or lattice, provides results that match these reference data very well.

For the profiles determined from hPF-MD snapshots, distinct oscillatory behavior is observed close to the vapor–liquid interface, with an amplitude that increases with the depth of the quench. This can be traced back to the fluctuating, particle-like nature of hPF-MD, which perturbs the profile when compared to the tanh-shape that is anticipated from mean-field theory. For this reason, we considered two methods to determine particle fractions f_ℓ and f_v in the liquid and vapor phases from simulated particle profiles. Since the area of the simulated liquid–vapor interface is small, damping of these oscillations by capillary waves, a phenomenon that can be expected based on findings in earlier studies, has not been considered.

For the $\tilde{\chi} - f$ phase diagram, we have confirmed invariance with respect to the effective particle volume v and the grid spacing ℓ . The latter agrees well with the observation that there is no true length scale in our setup. Only the maximum number of particles per grid cell ρ_0/v is found to play a more prominent role in the precision with which the SCF binodal is reproduced. This seems to be in agreement with the constraints associated with representation, which suggests that the field-based vapor fraction f_v cannot be captured by the underlying particle representation for large negative $\tilde{\chi}$, since this situation relates to less than one particle per grid cell on average.

We have tested two types of projections of particles to the field lattice: the usual cloud-in-cell, in which fractions of each particle are assigned to the eight direct lattice neighbors, and a procedure based on a Gaussian kernel that assigns the fractions to 64 neighbors by Gaussian weighing. We find that the projection based on a Gaussian kernel stabilizes our method, which becomes unstable for $f(\mathbf{r}) \geq 1$, and that the closest match to the reference binodal is identified for this projection and the highest considered ρ_0/v , i.e., for the effective field that is sampled by the largest amount of particle. Surprisingly, however, the match for much lower ρ_0/v to the reference values is also better than could be expected based on the above-mentioned representation issues.

Overall, however, one can always identify a small and varying mismatch between the binodal reconstructed by hPF-MD and the reference binodal from field theory. For multi-body DPD, a very similar mismatch between the input EOS and the one obtained by simulation was identified by Trofimov *et al.*² and treated by making a self-consistent correction to the density projection. Here, the mismatch is confirmed to vary with the projection method, so we could potentially employ a similar procedure. Yet, one should wonder if a perfect match is at all possible. Employing a quick method to estimate the critical exponent suggests that the exponent β for hPF-MD is not the one associated with a MF method ($\beta_{MF} = 0.5$), but closer to the $\beta = 0.325$ determined for a discrete (Ising) model. Additional study is clearly needed to address this point in detail. Meanwhile, we will adapt the current procedure to study a number of phenomena in compressible systems in the near future.

SUPPLEMENTARY MATERIAL

See the [supplementary material](#) for the procedure to determine the phase diagram, from the expression for the considered free energies, by numerical means and also the relevant hPF-MD results for the Cell Model in the form of simulated profiles and phase diagrams.

ACKNOWLEDGMENTS

The authors would like to thank Kostas Daoulas and Josep Bonet Avalos for stimulating and very useful discussions during the preparation of this manuscript. Moreover, Kostas made the valuable suggestion to implement MC in order to check the precision of the particle-based results in the absence of lattice-based operators.

DATA AVAILABILITY

The total amount of simulation data is quite considerable owing to the different sweeps that have been performed in determining the phase behavior. The data that support the findings of this study are available from the corresponding author upon reasonable request.

REFERENCES

- 1 I. Pagonabarraga and D. Frenkel, *J. Chem. Phys.* **115**, 5015 (2001).
- 2 S. Y. Trofimov, E. L. F. Nies, and M. A. J. Michels, *J. Chem. Phys.* **117**, 9383 (2002).
- 3 P. B. Warren, *Phys. Rev. E* **68**, 066702 (2003).
- 4 A. Ghoufi and P. Malfreyt, *Phys. Rev. E* **82**, 016706 (2010).
- 5 M. Müller and G. D. Smith, *J. Polym. Sci., Part B* **43**, 934 (2005).
- 6 K. C. Daoulas and M. Mueller, *J. Chem. Phys.* **125**, 184904 (2006).
- 7 G. Milano and T. Kawakatsu, *J. Chem. Phys.* **130**, 214106 (2009).
- 8 K. Katsov and J. D. Weeks, *J. Phys. Chem. B* **106**, 8429 (2002).
- 9 K. G. Soga, H. Guo, and M. J. Zuckermann, *Europhys. Lett.* **29**, 531 (1995).
- 10 Y. Norioze, K. C. Daoulas, and M. Müller, *Faraday Discuss.* **144**, 369 (2010).
- 11 K. C. Daoulas, M. Müller, J. J. de Pablo, P. F. Nealey, and G. D. Smith, *Soft Matter* **2**, 573 (2006).
- 12 M. Hömberg and M. Müller, *J. Chem. Phys.* **132**, 155104 (2010).
- 13 M. Hömberg and M. Müller, *Europhys. Lett.* **97**, 68010 (2012).
- 14 A. de Nicola, Y. Zhao, T. Kawakatsu, D. Roccatano, and G. Milano, *J. Chem. Theory Comput.* **7**, 2947 (2011).
- 15 N. M. Maurits, B. A. C. van Vlimmeren, and J. G. E. M. Fraaije, *Phys. Rev. E* **56**, 816 (1997).
- 16 M. Müller, *J. Stat. Phys.* **145**, 967 (2011).
- 17 G. J. A. Sevink, F. Schmid, T. Kawakatsu, and G. Milano, *Soft Matter* **13**, 1594 (2017).
- 18 S. W. Coles, D. Borgis, R. Vuilleumier, and B. Rotenberg, *J. Chem. Phys.* **151**, 064124 (2019).
- 19 Y. Zhao, A. De Nicola, T. Kawakatsu, and G. Milano, *J. Comput. Chem.* **33**, 868 (2012).
- 20 B. Leimkuhler and X. Shang, *J. Comput. Phys.* **280**, 72 (2015).
- 21 H. Watanabe, N. Ito, and C.-K. Hu, *J. Chem. Phys.* **136**, 204102 (2012).
- 22 J. S. Rowlinson and B. Widom, *Molecular Theory of Capillarity* (Clarendon, Oxford, 1982).
- 23 R. Evans, *Ber. Bunsenges. Phys. Chem.* **98**, 345 (1994).
- 24 F. P. Buff, R. A. Lovett, and F. H. Stillinger, *Phys. Rev. Lett.* **15**, 621 (1965).
- 25 R. J. Sadus, *J. Chem. Phys.* **115**, 1460 (2001).
- 26 K. Binder, *Z. Phys. B: Condens. Matter* **43**, 119 (1981).